



Mechanical and microstructural properties of S1100 UHSS welds obtained by EBW and MAG welding

Mustafa Tümer¹ · Florian Pixner² · Rudolf Vallant² · Josef Domitner² · Norbert Enzinger²

Received: 10 September 2021 / Accepted: 14 February 2022 / Published online: 22 March 2022
© International Institute of Welding 2022

Abstract

The microstructures and mechanical properties of welds consisting of 20-mm-thick thermo-mechanically rolled and directly quenched S1100MC ultra high-strength steel (UHSS) plates were investigated. The welds were produced by means of metal active gas (MAG) welding and electron beam welding (EBW). Different heat inputs of the welding processes influenced the microstructure and thus the mechanical properties including impact toughness, hardness, and tensile properties. The microstructure of the MAG weld obtained when using undermatched solid filler wire consisted mainly of acicular ferrite (AF), and it appeared more polygonal when the heat input exceeded 2 kJ/mm with spray arc in the filler pass. The coarse-grained heat-affected zone (CGHAZ) showed different microstructures depending on the thermal cycles of the respective welding processes. Fresh martensite formed in the CGHAZ of the last welding pass at both the bottom and the top surfaces, as there was no reheating from any subsequent pass. The microstructure obtained with EBW without any filler material consisted of martensite and tempered martensite in the fusion zone. Martensite with small prior austenite grain (PAG) size significantly increased the hardness of the fine-grained heat-affected zone (FGHAZ) compared to the CGHAZ and fusion zone. Uniaxial tensile testing of EBW specimens indicated higher tensile strength of the weld than of the base metal, as the specimens fractured at the base metal. In contrast, fracture of MAG specimens occurred at the weld. Hence, the tensile strength of the MAG weld consisting of undermatched filler metal was obviously lower than the tensile strength of the base metal. However, the ferritic MAG weld possessed higher impact toughness than the martensitic EBW weld.

Keywords MAG · EBW · UHSS · Microstructure · Mechanical properties · Strength · Toughness · Hardness

1 Introduction

Structural steels with yield strength beyond 700 MPa are generally classified as UHSS [1]. The continuous improvement of UHSS has shifted their mechanical properties toward higher limits. Therefore, these steels provide considerable advantages in terms of structural design and safety [2], weight reduction, and lower fuel consumption [3]. Consequently, products made from UHSS cause less emissions

[4]. However, in order to ensure these advantages, the weldability and the post-weld performance of UHSS must be evaluated in detail. The microstructure, which is mainly influenced by the welding process and its actual parameters, plays a key role for achieving acceptable mechanical properties of UHSS welds [5].

Thermo-mechanical rolling has nowadays been established as common process for producing UHSS. Steels produced by thermo-mechanically controlled processes comprise less carbon and higher microalloying elements than quenched and tempered steels, which may cause precipitation hardening [6]. Precipitation hardening is one of the most effective strengthening mechanisms in metallic materials, as high-density precipitations can effectively inhibit dislocation movement or twinning, which is beneficial to increase the strength of steel [7].

Arc welding processes are widely used for joining UHSS, and the yield strength of commercial filler metals has already exceeded 1000 MPa [8]. Multi-pass arc welding of thick

Recommended for publication by Commission IX - Behaviour of Metals Subjected to Welding

✉ Mustafa Tümer
mustafa.tumer@kocaeli.edu.tr

¹ Welding Technology Program, Kocaeli University, Kocaeli, Turkey

² Institute of Materials Science, Joining and Forming, Graz University of Technology, Graz, Austria

components causes microstructural changes in both the weld metal (WM) and the heat-affected zone (HAZ), which further affect the mechanical properties of the weldment [9, 10]. Although both laser and electron beam welding processes have limitations in terms of weldment dimensions, these processes show high potential for joining UHSS [11–13]. Compared to traditional arc welding processes, high-energy density welding processes have advantages such as high penetration depth and low specific heat input, which reduces the width of the HAZ and thermal distortion as well as residual stresses. The weld zone of an EBW joint is about six times thinner than the weld zone of a MAG joint [14]. However, it strongly depends on the weld joint design and properties of the GMAW process. Such as, narrow gap welding [15] and modified spray arc [16] can reduce noticeably size of weld metal deposition. In addition, structural steels, high-alloyed steels, non-ferrous metals, and even gas-sensitive special metals can be successfully welded using EBW [17]. However, the short cooling time (i.e., high cooling rates) may increase the hardness [18], decrease the toughness [19], and cause inhomogeneous properties of the fusion zone [20].

Cui et al. [21] reported that increasing the cooling time of the CGHAZ of high-strength steels changes the microstructure from martensite to bainite. Qi et al. [22] investigated microstructural changes inside the CGHAZ caused by the secondary thermal cycle in multi-pass welding. Due to the secondary thermal cycle necklace-type martensite-austenite (M-A) constituents, martensite, granular bainite, and AF are formed at 840 °C in the intercritical coarse-grained heat-affected zone (ICR-CGHAZ). For thermal cycles with peak temperature of 760 °C than of 840 °C, this zone was found to have lower toughness. Thus, increasing the peak temperature increases slightly the toughness in the intercritical CGHAZ. Keehan et al. [23] investigated mechanical properties of 20-mm-thick all weld metal test blocks. The blocks were produced by manual metal arc welding using filler metal having 922 MPa yield strength. They stated that the tensile strength and in particular the yield strength of the weld metal decrease with increasing cooling time. Additionally, Kovács and Lukács [24] simulated the section of HAZ of S1300 including ICR-CGHAZ using a physical simulator. In spite of the applied cooling time of 5 s, the hardness of the different HAZ sections did not reach the base metal hardness values.

The comparative analysis of microstructures, residual stresses, and mechanical properties after welding of UHSS produced by thermo-mechanically controlled processing and quenching and tempering has also been the subject of several studies [6, 11, 18, 25]. Schaupp et al. [6] proposed that local residual stresses in both the weld metal and the HAZ are mainly affected by phase transformations due to high heat input. Sisodia et al. [25] reported that the low heat input and high welding speed of EBW process induce more compressive residual stresses near the weld toe and HAZ for S960M steel than for S960QL steel. The problem of extreme hardness increase in the fusion zone of laser-welded UHSS was reported by Sun et al. [11] and Guo et al. [18].

In the present study, the microstructure and the mechanical properties of UHSS joints produced by MAG welding with an undermatched filler material and by EBW were compared. The results were evaluated and discussed in terms of phase transformation behavior and mechanical properties.

2 Experimental

2.1 Materials

Plates of thermo-mechanically rolled and directly quenched 20 mm-thick UHSS S1100MC were used as base metal. The dimensions of the plates to be welded with MAG and EBW in PA position were 500 mm × 150 mm and 300 mm × 150 mm, respectively. Böhler alform 960IG solid filler wire was used for MAG welding, but no filler metal was used for EBW. Chemical compositions, carbon equivalent values (CEV — according to EN ISO 1011–2) (<https://www.voestalpine.com/welding/Welding-Calculator>), and mechanical properties of the base metal and of the filler wire are listed in Table 1.

2.2 Welding equipment

In the MAG process, the Fronius TPS 400i power source was used. The welding torch was mounted on the arm of a six-axis articulated ABB IRB 140 robot. MAG welding was carried out in five passes using plates with an X-shaped weld bevel and Ar + 18 vol.% CO₂ as shielding gas without any preheating. The interpass temperature in the welding

Table 1 Chemical composition and mechanical properties of base metal S1100MC [26] and filler wire 960-IG [27]

Elements (wt.%)	C	Si	Mn	Cr	Ni	Mo	CEV	Yield strength- R _{p0.2} (MPa)	Tensile strength-R _m (MPa)	Fracture elongation- A ₅ (%)
voestalpine alform® 1100 x-treme	0.13	0.3	1.6	0.6	0.3	0.6	0.67	≥ 1100	1120–1300	8
Böhler alform® 960IG	0.12	0.80	1.90	0.45	2.35	0.55	0.79	≥ 930	≥ 980	≥ 14

experiments was ~ 90 °C. In the EBW process, the demagnetized plates were butt-welded using a pro-beam EBG 45–150 k14 electron beam welding machine with a maximum electron gun power of 45 kW. Prior to welding, the milled surfaces at the joint were cleaned and each plate was demagnetized to avoid beam deflection due to residual magnetization. The welding parameters and the derived nominal heat inputs for MAG multi-pass welding and for EBW single-pass welding are listed in Table 2. The nominal heat input was calculated by the equation, $Q = (U \times I) / s$ with given parameter. The macrostructure of the welds with schematic illustrations, which include the welding pass sequence, and the top view of weldments are shown in Fig. 1.

2.3 Microstructure characterization

Specimens extracted from the welded plates for microstructure examinations were ground, polished, and etched for 15 s using 3 vol.% Nital (HNO_3 + ethanol) solution. The microstructures of the specimens were analyzed using light optical microscopy (LOM), scanning electron microscopy (SEM), and electron backscatter diffraction (EBSD). A Zeiss Axio Observer optical microscope and a TESCAN MIRA-3 field emission scanning electron microscope (FESEM) equipped with an EDAX-Ametek EBSD and Hikari detector were used for detailed microstructure characterizations. EBSD analyses were performed for determining the grain boundary misorientation and the morphology (size and shape) of different phases within the weld zones. The orientation maps for EBSD were applied with the step size of 50 nm and the acceleration voltage of 20 kV. Orientation imaging microscopy (OIM) analysis software (version 8.0) was used for postprocessing the data. Misorientation angles larger than 15° were assigned to high angle grain boundary. Fine grains were identified from inverse pole figure (IPF) maps, image

quality (IQ), phase analysis, and kernel average misorientation (KAM) with 5° misorientation criteria.

2.4 Mechanical testing

Microhardness measurements were carried out using an automated EMCO-TEST DuraScan G5 hardness tester. The $\text{HV}_{0.2}$ hardness indentations in x - and y -direction were conducted with the dwell time of 10 s and with step sizes of 0.2 mm for the EBW specimen and 0.3 mm for the MAG specimen, respectively. Hardness tests were performed on half the cross-section of the MAG specimen and on the entire cross-section of the EBW specimen including base metal, HAZ, and WM. Notch impact testing at -40 °C and -20 °C was performed using three specimens extracted from the center of the fusion zone. The 1-mm-deep notch was located at the top surface of each specimen according to DIN EN ISO 9016 [31]. Moreover, specimens for tensile testing oriented perpendicular to the welding direction were machined out of the joints. Tensile tests according to DIN EN ISO 6892–1 [32] were performed on three samples at room temperature using a 400 kN Amsler UPM F29 tensile testing device. The constant testing velocity was 4 mm/min.

3 Results and discussion

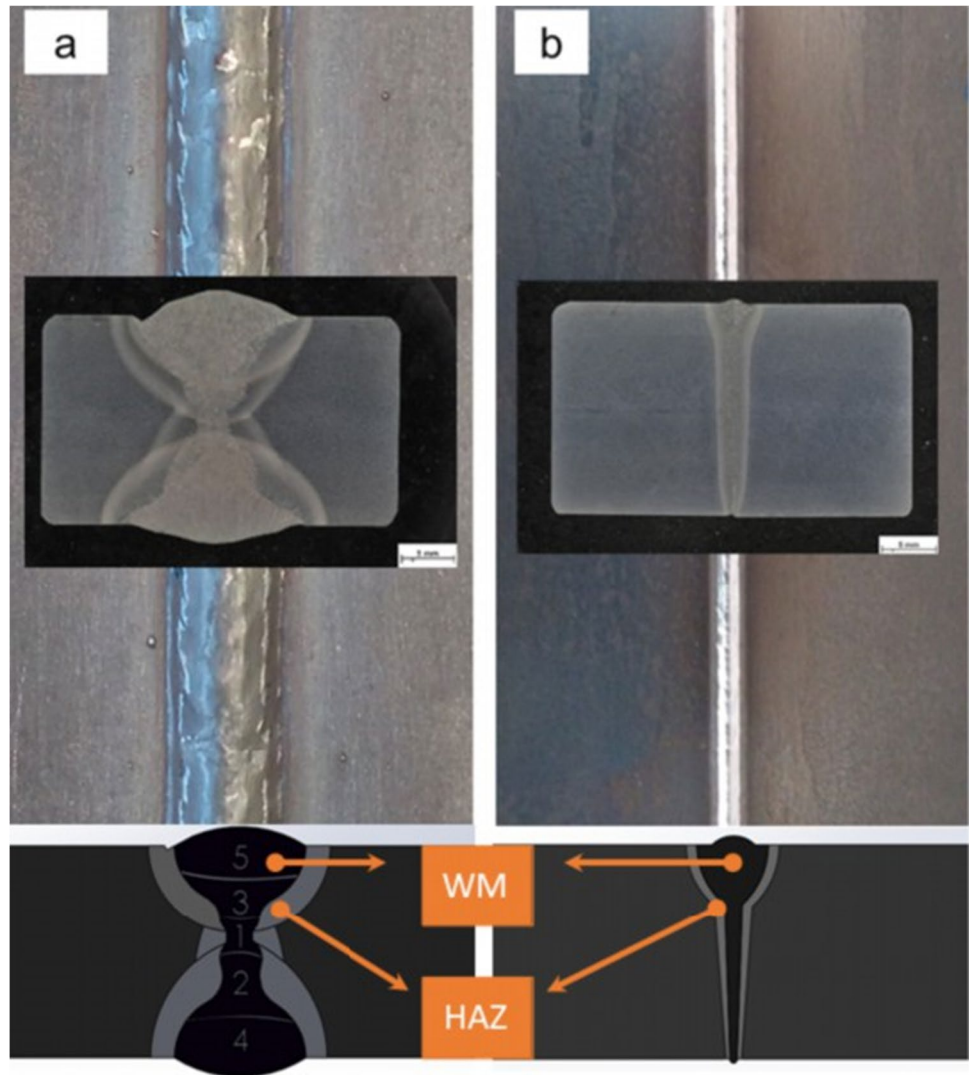
3.1 Microstructure of weld metal

For investigating the effect of the heat input on the microstructure of each weld, four different regions were considered: (A) the top and the bottom regions of the weld metal of the MAG specimen, i.e., the 4th and 5th welding pass; (B) the reheated and non-reheated CGHAZ of the MAG specimen; (C) the fusion zone of the EBW specimen; and (D)

Table 2 Welding parameters of MAG [28] multi-pass welding and EBW [29] single-pass welding

Welding processes	MAG	Pass number	Welding current (A)	Welding voltage (V)	Wire speed (m/min)	Welding speed (s) (mm/s)	Nominal heat input Q (kJ/mm)
		1	179.5	17.05	4.7	5	0.61
		2	310	28.95	8.3	5	1.79
		3	314	29	8.3	5	1.82
		4	298.5	29.05	8.3	4	2.17
		5	280	26	8	5	1.46
	EBW	Diameter of deflection (mm)	Beam current (mA)	Acceleration voltage (kV)	Oscillation frequency (kHz)	Welding speed (mm/s)	Nominal heat input (kJ/mm)
		0.5	63	120	1	12	0.63

Fig. 1 Cross-sections images/schematic illustrations and top views of **a** MAG [28] and **b** EBW [30] joints

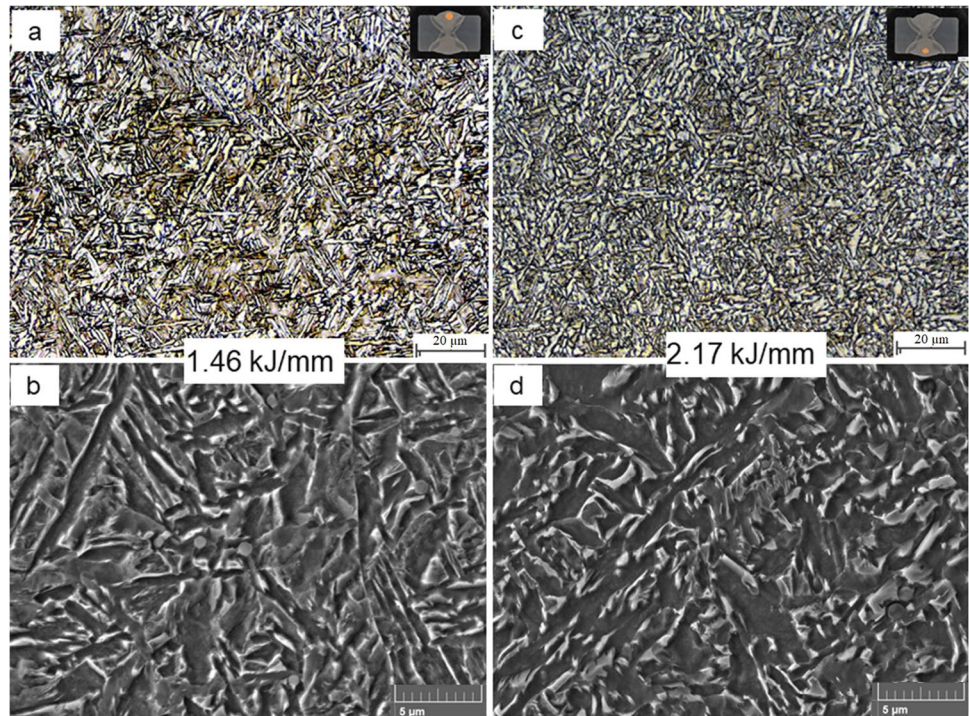


the CGHAZ of the EBW specimen. The associated cooling time according to EN ISO 1011–2, $t_{8/5}$, was estimated with the voestalpine weld calculator utilizing 0.9 shape factor (<https://www.voestalpine.com/welding/Welding-Calculator>). $t_{8/5}$ was 8.9 s for the 5th MAG welding pass, 18.3 s for the 4th welding MAG pass, and 3.0 s for the EBW weld, respectively. The recommended $t_{8/5}$ cooling time range for the 960-IG is between 3 and 15 s and interpass temperature should be below 150 °C according to data sheet [33]. However, the recommendations are generally difficult to comply with, since the MAG process aims at a high material deposition rate, i.e., also a high energy input. The microstructures of the 4th and 5th welding pass are depicted in Fig. 2. While the weld metal in the 5th pass consisted of very fine AF, the microstructure in the 4th pass was mainly polygonal ferrite. The average heat inputs of the 4th and the 5th pass were 2.17 kJ/mm and 1.46 kJ/mm, respectively. The polygonal ferrite (PGF) structure, which formed in the 4th pass, can be attributed to the effect of spray arc with higher arc force and

lower welding speed than in the 5th pass. Furthermore, the ferrite structure is promoted by high peak temperature and long cooling time due to the comparatively high heat input. The gradual transformation of AF to PGF with increasing heat input was also reported by Kim et al. [34]. However, a decrease in hardness must be expected in regions with PGF [35].

In contrast to the ferrite-dominated microstructure of the MAG weld, the EBW microstructure consisted of martensite and tempered martensite (Fig. 3). The tempered martensite in the single-pass EBW process can be attributed to the phenomenon of auto-tempering during slow cooling in a low temperature range. Martensite can be formed by diffusionless transformation even at low temperatures when austenized low alloy steel is rapidly cooled. Carbon atoms that were completely dissolved in the austenite prior martensite transformation become supersaturated in the body-centered cubic matrix after martensite formation. In vacuum-based EBW processes, heat is dissipated mainly

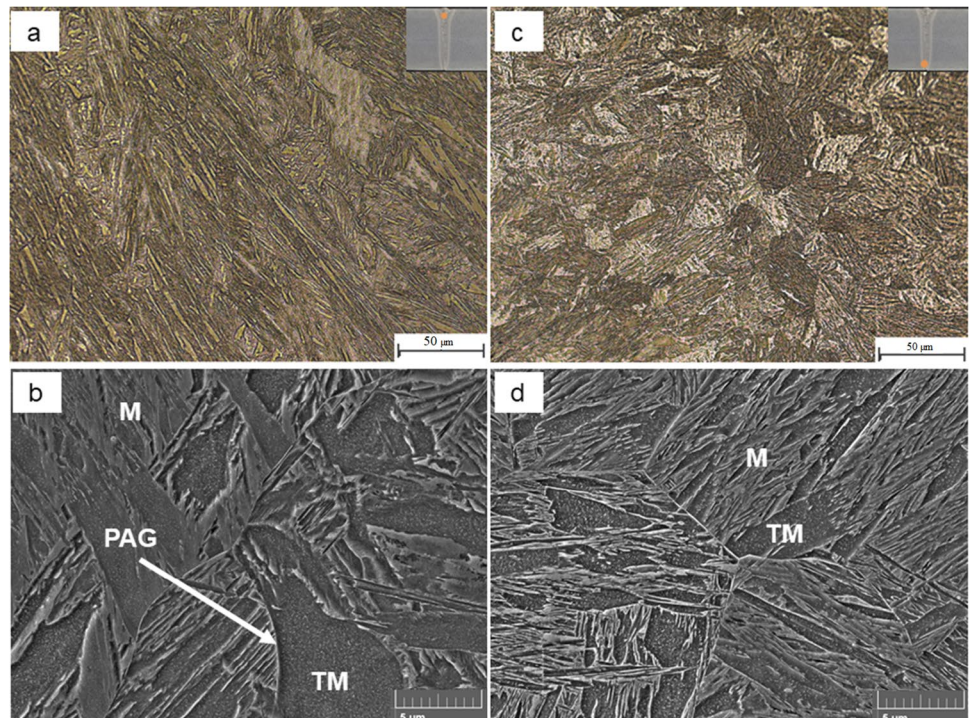
Fig. 2 Microstructures of (a, b) 5th and (c, d) 4th MAG μ m welding passes



by thermal radiation without convection. Therefore, and according to the Stefan-Boltzmann law, heat is dissipated fast by radiation at higher temperatures and rather slowly at lower temperatures, i.e., within the range of martensite start (M_s) temperature. Even at low temperatures and very high cooling rates, the mobility of carbon in ferrite is sufficient

for formation and growth of cementite within the formed martensite lamellar [30]. Due to higher contents of alloying elements in UHSS, the M_s temperature is higher [18]. Hence, larger amount of martensite forms at higher temperatures during the cooling process, which further enhances and promotes the auto-tempering behavior.

Fig. 3 Microstructures of EBW welds at (a, b) face and (c, d) root regions



Comparing the weld metals obtained with both welding processes in terms of microstructural transformations leads to the following observations: first, due to the composition of the filler metal and the relatively long cooling time of the weld metal, martensitic microstructures are not expected to form during MAG welding. Second, EBW causes very rapid cooling, which promotes the formation of martensite in the fusion zone consisting of solidifying base metal. Therefore, the formation of bainite and of derivative phases in the microstructure is suppressed. However, different heat inputs of the EBW and MAG welding processes as well as of the MAG welding passes resulted in local differences in the microstructure with respect to the PAG. Since the solidification from the fusion line to the weld centerline occurs with different retardation on the face side compared to the root side in EBW welding, the face side has a longer cooling time than the root area; due to this fact, the PAGs increased from the root to the face side [30].

Selected areas of the weld metal microstructures of the 4th and 5th MAG welding pass and of the face area of the EBW weld were used for further examinations and for plotting the IPF orientation maps, phase fraction maps and KAM maps as shown in Fig. 4.

While comparatively fine AF was observed in the 5th MAG welding pass (Fig. 4a), coarser AF and predominantly PGF were observed in the 4th pass (Fig. 4d). The maps indicate that the EBW fusion zone (Fig. 4g) consists of lath and tempered martensite in different orientations. Figure 4b–h show the phase distribution of the weld metals. Small blocks of retained austenite (phase fraction of 2.4%, Table 3) are mainly present in the 4th MAG welding pass within regions of AF and PGF. Wang et al. reported that retained austenite occurs in the microstructure of high-strength weld metals when the annealing temperature is slightly higher than the A_{c1} temperature [36]. This is due to the redistribution of alloying elements and the enrichment of Mn and Ni in the retained austenite. The distribution of retained austenite in the weld metal was inhomogeneous, as its phase fraction was significantly higher in the 4th pass (high heat input), than in the 5th pass (low heat input). The presence of considerable amounts of retained austenite in the microstructure of high-strength steels may also improve the toughness and the resistance to hydrogen embrittlement [37].

KAM maps were used for studying the local stress distribution inside the microstructure [38]. KAM maps illustrate high misorientation in the EBW specimen (yellow and red areas in Fig. 4i), which indicates that EBW causes relatively high concentrations of (residual) stresses. However, the martensitic microstructure of the EBW fusion zone exhibits a more homogeneous stress distribution than the microstructures of the MAG weld. The coarser microstructures of the 4th (Fig. 4c) and the 5th (Fig. 4f) MAG welding pass show

local concentrations of high misorientations, which may also indicate partial stress relief in the microstructure.

3.2 Microstructure of heat-affected zone

Light optical micrographs at lower magnification from the root, middle, and face regions of the HAZ of EBW and MAG welds are shown in Fig. 5. Different heat input, thermal cycles, and exposure time at peak temperature caused different widths of the HAZ. In addition, different sections of the HAZ are distinguished depending on the exposure time at certain temperatures: CGHAZ (coarse-grained), FGHAZ (fine-grained), ICHAZ (intercritical), and SCHAZ (subcritical). The CGHAZ of the 5th MAG welding pass has about 1.6 mm in width (Fig. 5a), while the comparatively narrow CGHAZ formed in EBW has only about 0.5 mm at the face area (Fig. 5d–f). In other words, the CGHAZ obtained with the MAG arc welding process is about three times wider than the HAZ obtained with the high-power density EBW process.

Thermal cycles of subsequent MAG welding passes caused reheating and microstructural transformations (Fig. 5a–c). Hence, a complex microstructure forms in multi-pass welds. Combinations of CGHAZ and ICHAZ may occur when the CGHAZ is heated by secondary thermal cycles to temperatures between A_{c1} and A_{c3} . This region, which contains martensite, tempered martensite, and low-temperature transformation products such as M-A constituents and bainite, is called intercritical coarse-grained HAZ (ICR-CGHAZ) [22, 39, 40].

The microstructure of the CGHAZ is shown in Fig. 6. Measurements using thermocouples revealed that this region was exposed to peak temperature of 1150 °C during the welding process. Therefore, temperature- and time-dependent growth of austenite grains occurred [4]. Due to the short cooling time (i.e., the rapid cooling rates), the microstructure of the CGHAZ obtained with MAG and EBW consists of martensite (M) and tempered martensite (TM) of different prior austenite grain (PAG) size. Since grain growth is a temperature- and time-dependent event, the PAG size is generally smaller for EBW than for MAG welds.

Figure 7 shows the ICR-CGHAZ subjected to multiple thermal cycles during MAG multi-pass welding. In multi-pass welding of thick steel cross-sections, the CGHAZ is typically tempered at 750–850 °C [41]. Necklace-type M-A constituents are constantly formed in the ICR-CGHAZ of high-strength steels [42]. The size and distribution of M-A constituents is influenced by the PAG and thus by the time and temperature of tempering [43]. Microstructural changes in the ICR-CGHAZ are evident, as the grains are about ten times larger than the grains in the ICHAZ. Depending on the particular peak temperatures of subsequent welding passes, the matrix consisted predominantly of bainite (B) with M-A

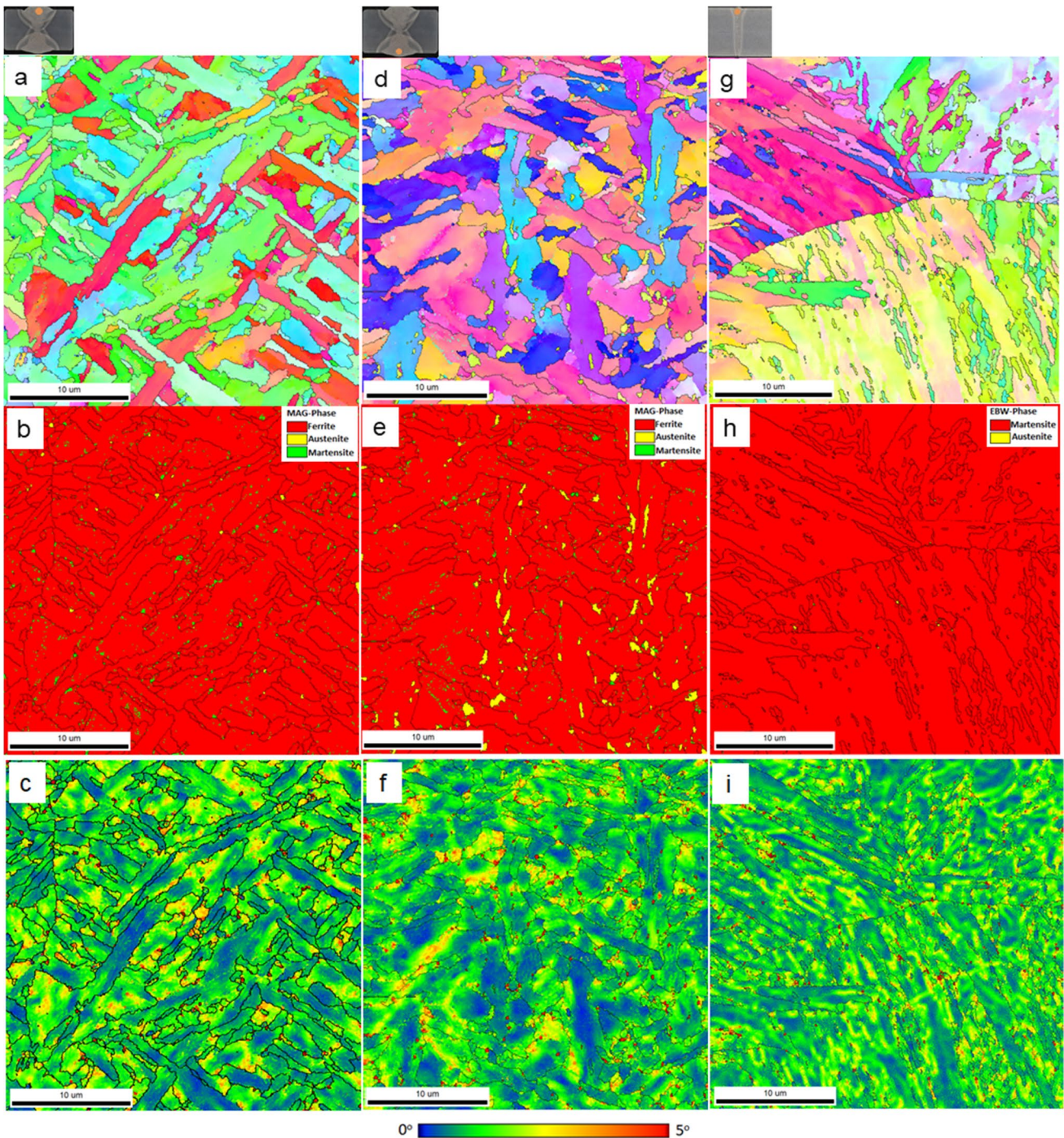


Fig. 4 IPF maps, phase fraction maps, and KAM maps of MAG and EBW welds: (a–c) 5th MAG pass, (d–f) 4th MAG pass, (g–i) EBW weld

Table 3 Phase fractions for EBW and MAG welds determined using EBSD

Phase (%)	EBW	MAG (5 th pass)	MAG (4 th pass)
Ferrite	–	98.1	96.2
Austenite	0.1	0.2	2.4
Martensite	99.9	1.7	1.4

constituents at the boundaries (Fig. 7c). M-A constituents, which can be formed by rapid heating and subsequent cooling due to carbon enrichment during thermal welding cycles, influence the toughness of the ICR-CGHAZ [44]. The deterioration of toughness of the ICR-CGHAZ can be due to enrichments of carbon and manganese in M-A constituents, which may promote the detachment of M-A constituents

Fig. 5 Microstructure of the entire HAZ of the (a–c) MAG and (d–f) EBW welds

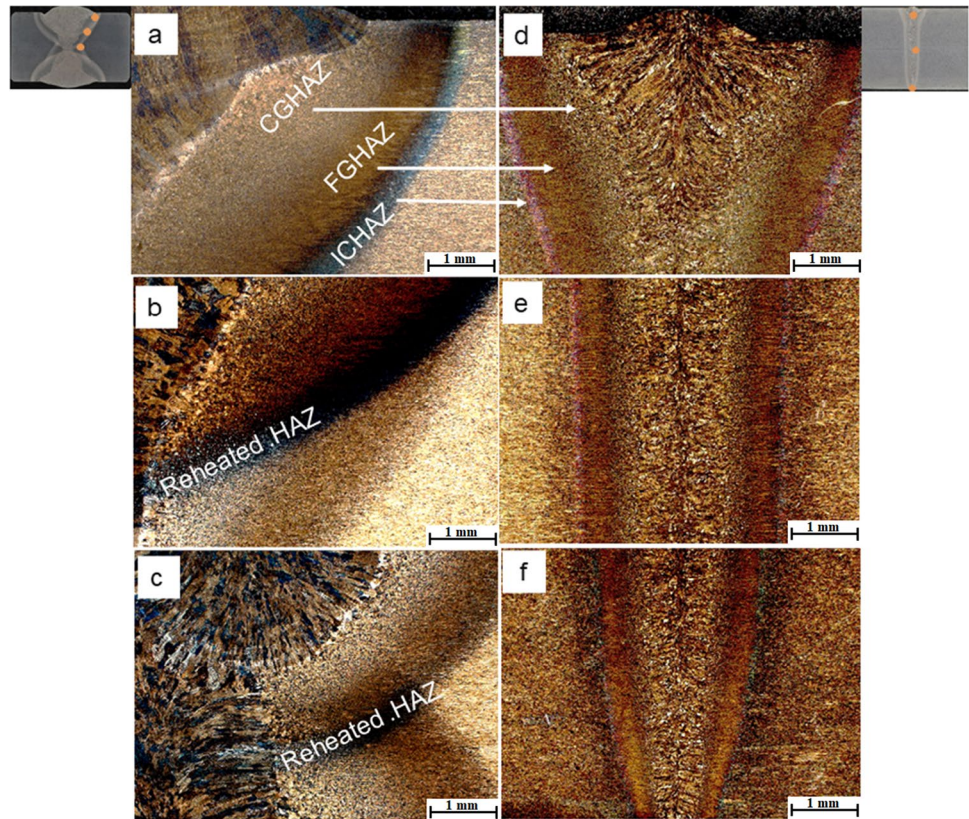


Fig. 6 Microstructure of the CGHAZ of the (a) MAG and (b) EBW welds

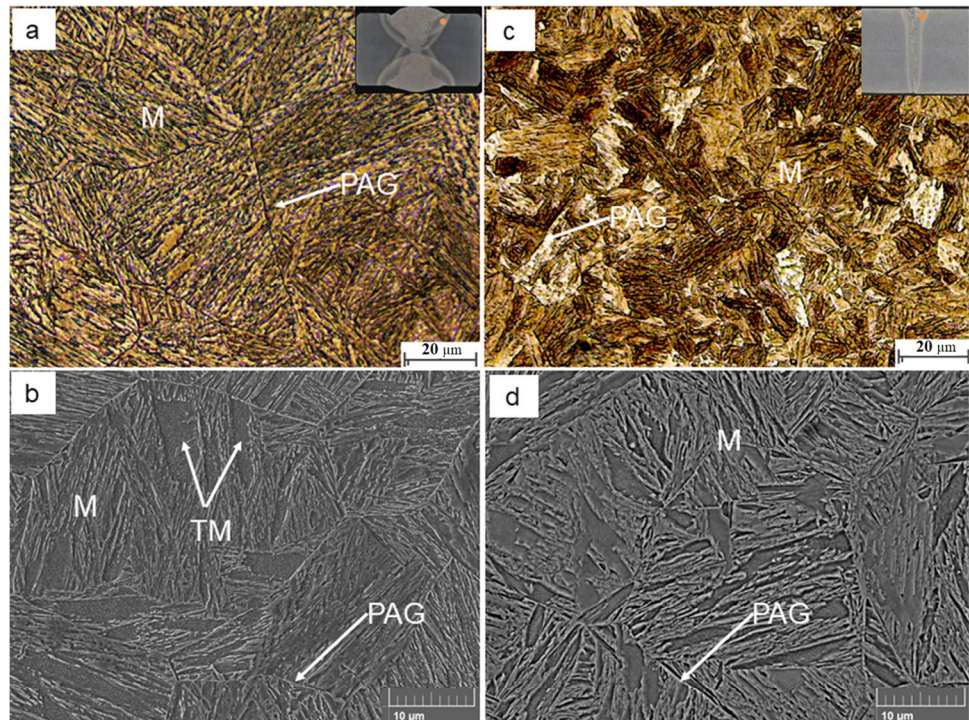
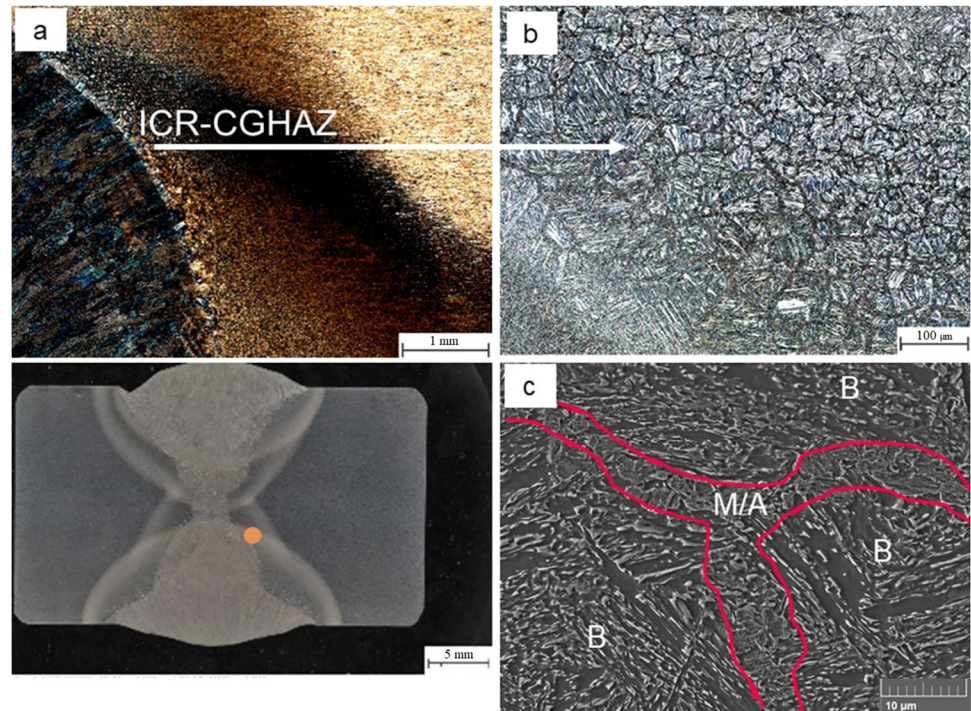


Fig. 7 Microstructure of the ICR-CGHAZ of the MAG weld



from the matrix and initiate the nucleation of cleavage cracks [22, 40]. However, a high secondary peak temperature can increase the impact energy/toughness of the ICR-CGHAZ due to bainitic transformations beyond 800 °C [22].

3.3 Hardness

Due to differences in thermal characteristics of arc welding and high-power density welding processes, the phase transformations in the fusion zone and in the HAZ, and thus also the hardness distribution of the joints are significantly affected. Due to the repeated heat input and the slow cooling rate as well as the chemical composition of the filler metal, softening is inevitable in the MAG process both in the weld metal and in certain zones of the HAZ. Moreover, the transformations that occur in the weld metal of such steels as a function of the cooling time lead to a decrease in hardness with increasing heat input [13] and vice versa, i.e., to an increase in hardness with decreasing heat input [9]. Since the rapid cooling of the EBW process supports the chaotic martensite structure in this steel grade, this leads to higher hardness values in the FZ and HAZ than in the base metal, so that similar hardness values for UHSS welded by the laser welding process have been reported in previous studies [12, 13].

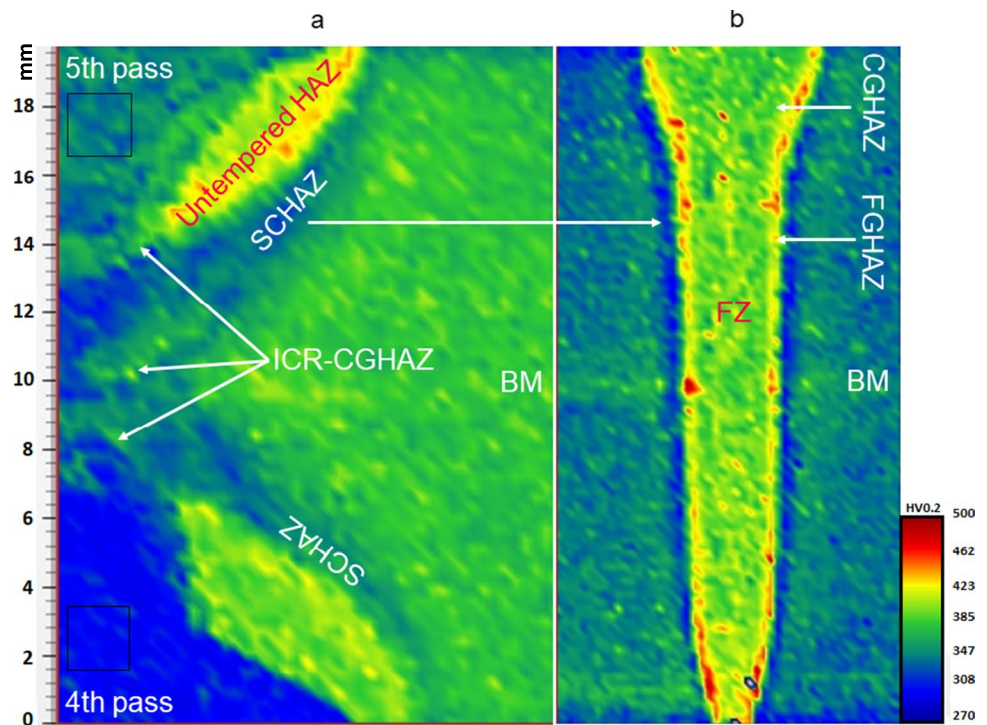
Figure 8 shows microhardness maps of MAG and EBW joints. Hardness differences across base metal, HAZ, and fusion zone are obvious. The average hardness of the base metal is about 380 HV_{0.2}. The spray arc-related high energy input during the 4th MAG welding pass caused high peak

temperature and slow cooling of the comparatively wide weld pool. Hence, PGF of the 4th pass was different to the AF of the 5th pass. Due to this difference in morphology, the average hardness of the weld metal was significantly lower for the 4th pass (about 310 HV_{0.2}) than for the 5th pass (about 345 HV_{0.2}). In comparison, the average hardness of the EBW fusion zone is about 420 HV_{0.2}, which is approximately 10% higher than the average hardness of the base metal. This is mainly due to the fully martensitic microstructure which forms at the high cooling rate of the EBW process.

The HAZ of the 5th MAG welding pass close to the surface consisted of untempered martensite with high average hardness of about 420 HV_{0.2}, which is comparable to the hardness of the EBW fusion zone. The hardness of the HAZ next to the last weld bead subjected to reheating was about 400 HV_{0.2}. The HAZ of the root and filler beads consisted of tempered martensite and M-A constituents, which have partly lower hardness than the base metal. This is mainly due to multiple thermal cycles that annealed the already deposited weld metal during subsequent welding passes at low peak temperatures.

CGHAZ and fusion zone of the EBW joints have almost identical microstructures, and there were no significant differences in hardness. Smaller PAG size and martensitic phases resulted in high peak hardness (about 460 HV_{0.2}) of the FGHAZ. The SCHAZ, which does not show any metallographic indicator, is typically exposed to peak temperatures of 450–700 °C [41, 45]. Recovery phenomena and decomposition of martensite could occur in this temperature range. When the steel is heated above the martensite start

Fig. 8 Hardness maps of (a) MAG [28] and (b) EBW joints [30]



(Ms) temperature, carbides are assumed to precipitate from the martensitic phase and agglomerate at the grain boundaries. The dislocation density of the microstructure may decrease and phase transformations [20] depending on the peak temperature and exposure time may occur [46]. Since high dislocation densities [47] and high volume fractions of carbides [7] tend to increase the hardness of martensitic steel, the actual low hardness of the SCHAZ could be mainly attributed to the reduction in dislocation density. The low heat input of the EBW process resulted in a very narrow SCHAZ. However, since the SCHAZ has similar hardness in both MAG and EBW (about 360 HV_{0.2}), it can be concluded that the heat input does not affect the hardness but the width of the SCHAZ.

3.4 Tensile properties

The average tensile properties of the MAG and EBW joints are listed in Table 4. Both the yield strength and the tensile strength of the EBW joint are higher than the minimal nominal strength values of the base metal. Consequently, fracture occurred in the base metal with an average fracture

elongation of 20.6% in the EBW samples. Compared to the minimum nominal strength of the base metal, the strength of the MAG joint was lower. Furthermore, the fracture took place in the weld metal due to the use of undermatched filler metal. However, the strength similar to the initial strength of the filler wire (yield strength ≥ 930 MPa and tensile strength ≥ 980 MPa, Table 1) was achieved.

3.5 Impact toughness

The results of the Charpy V-notch impact toughness tests are shown graphically including error bars (negative and positive extreme values) in Fig. 9. The average impact toughness of the EBW specimens is lower than the average impact toughness of the MAG specimens. That is mainly attributed to the EBW microstructure providing high strength and hardness in the fusion zone. For the EBW samples, energy absorption of 19.6 ± 1.7 J and 20.3 ± 1.7 J was determined at -40 °C and -20 °C, respectively. Since these values are below the minimum of 27 J required at -20 °C, the EBW joints in the as-welded condition do not meet the requirements with respect to impact toughness. Post-weld processing of the

Table 4 Tensile properties of MAG [28] and EBW [30] joints of S1100MC steel

Welding process	Yield strength R _{p0.2} (MPa)	Tensile strength R _m (MPa)	Fracture elongation A ₅ (%)	Fracture location
MAG	1019 ± 3	1142 ± 1	11.8 ± 0.6	Weld metal
EBW	1174 ± 15	1247 ± 2.2	20.6 ± 0.8	Base metal

EBW joints, such as post-weld heat treatment, would be needed to meet the requirements. Impact toughness tests of the MAG welds were performed with specimens extracted between the 3rd and the 5th MAG welding pass. Since the microstructure of these weld passes is predominantly AF, the MAG weld has superior energy absorption of 50 ± 0.8 J and 55 ± 1.9 J at -40 °C and -20 °C, respectively.

As shown in Fig. 10, fracture surfaces of EBW and MAG specimens tested at -20 °C (energy absorption of 22 J and 56 J) were examined using SEM. Owing to the fundamentally different microstructures of the MAG and EBW welds, the macroscopic appearance of the fracture surfaces (Fig. 10a and d) differs considerably. The MAG

specimen shows lateral expansion of 1.9 mm due to ductile fracture and plastic deformation in the peripheral area (Fig. 10b). Quasi-cleavage fracture with ductile fracture columns occurred at the edges of the specimen (Fig. 10c). In contrast, the EBW specimen exhibits a predominantly brittle fracture surface without distinct macroscopic lateral expansion. However, local ductile fracture occurred at the crack initiation area (Fig. 10e), which is partially characterized by the presence of fine dimples. Brittle fracture of the martensitic fusion zone and numerous secondary cracks were observed in the region of crack propagation (Fig. 10f).

Fig. 9 Impact toughness of EBW [30] fusion zone and MAG [28] weld metal

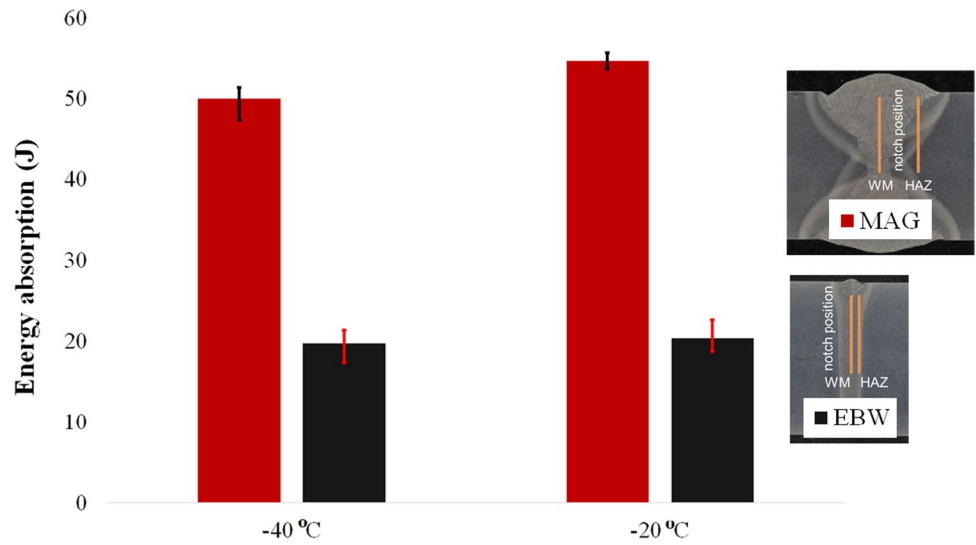
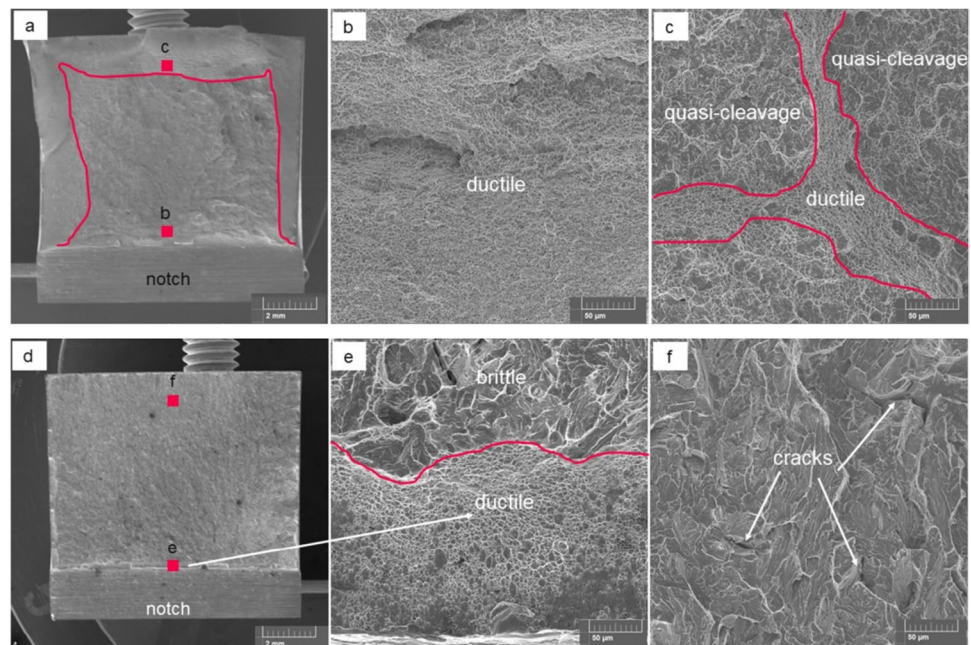


Fig. 10 Fracture surfaces of Charpy V-notch specimens of (a, b, c) MAG and (d, e, f) EBW welds



4 Conclusions

The present work investigates microstructures and mechanical properties of joints of 20 mm-thick S1100MC UHSS plates produced by means of EBW without filler and MAG welding with undermatched filler wire. Based on the results, the following conclusions can be drawn:

- (1) Fine-grained ferrite was dominant in the microstructure of the MAG weld. The morphology of the ferrite was mainly influenced by the heat input. Moreover, reheating the weld metal due to multi-pass welding formed a large amount of necklace-type M-A constituents particularly in ICR-CGHAZ.
- (2) The MAG weld, consisting mainly of fine-grained AF, possessed acceptable impact toughness. Tensile stress and yield stress of the weld metal produced using the undermatched filler wire were slightly lower than those of the base metal.
- (3) Heat distribution and hence PAG varied from the face to the root of the EBW weld. The FGHAZ consisted of martensite with rather small PAG. This zone exhibited the highest hardness within a very narrow region along the joint.
- (4) Due to the martensitic microstructure of the EBW fusion zone, the energy absorption of the EBW weld was below the required minimum of 27 J at $-20\text{ }^{\circ}\text{C}$. However, since the tensile strength of the fusion zone was higher than the minimal nominal strength of the base metal, fracture occurred entirely in the base metal.

Acknowledgements Base metal and filler wire were provided by voestalpine Stahl Linz and voestalpine Böhler Welding, respectively. The authors would like to thank Heinz Karl Fasching, Leander Herbitschek, Zahra Silvayeh, and Fernando Gustavo Warchomicka for their assistance with the experiments.

Funding Mustafa Tümer was supported by The Scientific and Technological Research Council of Turkey (TUBITAK) under the 2219 International Postdoctoral Research Scholarship Program.

Declarations

Conflict of interest The authors declare no competing interests.

References

1. Amraei M, Afkhami S, Javaheri V, Larkiola J, Skriko T, Björk T, Zhao XL (2020) Mechanical properties and microstructural evaluation of the heat-affected zone in ultra-high strength steels. *Thin-Walled Struct* 157:1–11. <https://doi.org/10.1016/j.tws.2020.107072>
2. Qiang X, Jiang X, Bijlaard FSK, Kolstein H (2016) Mechanical properties and design recommendations of very high strength steel S960 in fire. *Eng Struct* 112:60–70. <https://doi.org/10.1016/j.engstruct.2016.01.008>
3. Nowacki J, Sajek A, Matkowski P (2016) The influence of welding heat input on the microstructure of joints of S1100QL steel in one-pass welding. *Arch Civ Mech Eng* 16:777–783. <https://doi.org/10.1016/j.acme.2016.05.001>
4. Mičian M, Harmaniak D, Nový F, Winczek J, Moravec J, Trško L (2020) Effect of the t8/5 cooling time on the properties of S960MC steel in the HAZ of welded joints evaluated by thermal physical simulation. *Metals (Basel)* 10:18. <https://doi.org/10.3390/met10020229>
5. Węglowski MS, Błacha S, Dymek S, Kopyściański M (2017) Electron beam welding of high strength quenched and tempered steel. *Mater Sci Forum* 879:2078–2083. <https://doi.org/10.4028/www.scientific.net/MSF.879.2078>
6. Schaupp T, Schroepfer D, Kromm A, Kannengiesser T (2014) Welding residual stress distribution of quenched and tempered and thermo-mechanically hot rolled high strength steels. *Adv Mater Res* 996(457):462. <https://doi.org/10.4028/www.scientific.net/AMR.996.457>
7. Sun J, Wei S, Lu S (2020) Influence of vanadium content on the precipitation evolution and mechanical properties of high-strength Fe–Cr–Ni–Mo weld metal. *Mater Sci Eng A* 772:138739. <https://doi.org/10.1016/j.msea.2019.138739>
8. An T, Wei J, Zhao L, Shan J, Tian Z (2019) Influence of carbon content on microstructure and mechanical properties of 1000 MPa deposited metal by gas metal arc welding. *J Iron Steel Res Int* 26(512):518. <https://doi.org/10.1007/s42243-019-00270-6>
9. Haslberger P, Ernst W, Schneider C, Holly S, Schnitzer R (2018) Influence of inhomogeneity on several length scales on the local mechanical properties in V-alloyed all-weld metal. *Weld World* 62:1153–1158. <https://doi.org/10.1007/s40194-018-0636-0>
10. Laitila J, Larkiola J (2019) Effect of enhanced cooling on mechanical properties of a multipass welded martensitic steel. *Weld World* 63:637–646. <https://doi.org/10.1007/s40194-018-00689-7>
11. Sun Q, Di HS, Li JC, Wu BQ, Misra RDK (2016) A comparative study of the microstructure and properties of 800 MPa microalloyed C-Mn steel welded joints by laser and gas metal arc welding. *Mater Sci Eng A* 669:150–158. <https://doi.org/10.1016/j.msea.2016.05.079>
12. Guo W, Crowther D, Francis JA, Björk T, Heidarpour A, Zhao XL (2015) Microstructure and mechanical properties of laser welded S960 high strength steel. *Mater Des* 85:534–548. <https://doi.org/10.1016/j.matdes.2015.07.037>
13. Amraei M, Ahola A, Afkhami S, Björk T, Heidarpour A, Zhao XL (2019) Effects of heat input on the mechanical properties of butt-welded high and ultra-high strength steels. *Eng Struct* 198:109460. <https://doi.org/10.1016/j.engstruct.2019.109460>
14. Błacha S, Węglowski MS, Dymek S, Kopyściański M (2016) Microstructural characterization and mechanical properties of electron beam welded joint of high strength steel grade S690QL. *Arch Metall Mater* 61:1193–1200. <https://doi.org/10.1515/amm-2016-0198>
15. Agrawal BP, Ghosh PK (2017) Characteristics of extra narrow gap weld of HSLA steel welded by single-seam per layer pulse current GMA weld deposition. *J Mater Eng Perform* 26:1365–1381. <https://doi.org/10.1007/s11665-017-2516-y>
16. Schaupp T, Rhode M, Kannengiesser T (2018) Influence of welding parameters on diffusible hydrogen content in high-strength steel welds using modified spray arc process. *Weld World* 62:9–18. <https://doi.org/10.1007/s40194-017-0535-9>
17. Węglowski MS, Błacha S, Phillips A (2016) Electron beam welding-techniques and trends-review. *Vacuum* 130:72–92. <https://doi.org/10.1016/j.vacuum.2016.05.004>
18. Guo W, Li L, Dong S, Crowther D, Thompson A (2017) Comparison of microstructure and mechanical properties of ultra-narrow

- gap laser and gas-metal-arc welded S960 high strength steel. *Opt Lasers Eng* 91:1–15. <https://doi.org/10.1016/j.optlaseng.2016.11.011>
19. Schneider C, Ernst W, Schnitzer R, Staufer H, Vallant R, Enzinger N (2018) Welding of S960MC with undermatching filler material. *Weld World* 62:801–809. <https://doi.org/10.1007/s40194-018-0570-1>
 20. Xu J, Peng Y, Guo S, Zhou Q, Zhu J, Li X (2019) Softening behavior of electron beam welded 22SiMn2TiB steel. *J Mater Eng Perform* 28:6669–6681. <https://doi.org/10.1007/s11665-019-04366-8>
 21. Cui J, Zhu W, Chen Z, Chen L (2020) Effect of simulated cooling time on microstructure and toughness of CGHAZ in novel high-strength low-carbon construction steel. *Sci Technol Weld Join* 25:169–177. <https://doi.org/10.1080/13621718.2019.1661116>
 22. Qi X, Di H, Wang X, Liu Z, Misra RDK, Huan P, Gao Y (2020) Effect of secondary peak temperature on microstructure and toughness in ICCGHAZ of laser-arc hybrid welded X100 pipeline steel joints. *J Mater Res Technol* 9:7838–7849. <https://doi.org/10.1016/j.jmrt.2020.05.016>
 23. Keehan E, Zachrisson J, Karlsson L (2010) Influence of cooling rate on microstructure and properties of high strength steel weld metal. *Sci Technol Weld Join* 15:233–238. <https://doi.org/10.1179/136217110X12665048207692>
 24. Kovács J, Lukács J (2021) Effect of the welding thermal cycles based on simulated heat affected zone of S1300 ultrahigh strength steel. *Key Eng Mater* 890:33–43. <https://doi.org/10.4028/www.scientific.net/KEM.890.33>
 25. Sisodia RPS, Gáspár M, Seps M, Mertinger V (2021) Comparative evaluation of residual stresses in vacuum electron beam welded high strength steel S960QL and S960M butt joints. *Vacuum* 184:1–5. <https://doi.org/10.1016/j.vacuum.2020.109931>
 26. Voestalpine Steel (2019) Superior solutions in high-strength and ultra-high strength TM steel. Data sheet
 27. Böhler Welding (2014) BÖHLER alform® 960-IG Solid wire, high strength. Data sheet
 28. Tümer M, Warchomicka FG, Pahr H, Enzinger N (2022) Mechanical and microstructural characterization of solid wire undermatched multilayer welded S1100MC in different positions. *J Manuf Process* 73:849–860. <https://doi.org/10.1016/j.jmapro.2021.11.021>
 29. Tümer M, Domitner J, Enzinger N (2021) Electron beam and metal active gas welding of ultra-high-strength steel S1100MC: influence of heat input. *Int J Adv Manuf Technol*. <https://doi.org/10.1007/s00170-021-08055-6>
 30. Tümer M, Pixner F, Enzinger N (2021) Residual stresses, microstructure and mechanical properties on electron beam welded S1100 steel. *J Mater Eng Perform*. <https://doi.org/10.1007/s11665-021-06348-1>
 31. DIN EN ISO 9016 (2012) Destructive tests on welds in metallic materials-impact tests-test specimen location, notch orientation and examination. European Committee for Standardization
 32. DIN EN ISO 6892-1 (2016) Metallic materials-tensile testing-part 1: method to test at room temperature. European Committee for Standardization
 33. voestalpine Grobblech GmbH (2020) High-strength and ultra-high-strength thermomechanically rolled fine-grained steels - Technical terms of delivery for heavy plates. Data sheet
 34. Kim B, Uhm S, Lee C, Lee J, An Y (2005) Effects of inclusions and microstructures on impact energy of high heat-input submerged-arc-weld metals. *J Eng Mater Technol* 127:204–213. <https://doi.org/10.1115/1.1857933>
 35. Alipooramirabad H, Ghomashchi R, Paradowska A, Reid M (2016) Residual stress-microstructure-mechanical property interrelationships in multipass HSLA steel welds. *J Mater Process Technol* 231:456–467. <https://doi.org/10.1016/j.jmatprotec.2016.01.020>
 36. Wang XL, Wang XM, Shang CJ, Misra RDK (2016) Characterization of the multi-pass weld metal and the impact of retained austenite obtained through intercritical heat treatment on low temperature toughness. *Mater Sci Eng A* 649:282–292. <https://doi.org/10.1016/j.msea.2015.09.030>
 37. Khodir S, Shibayanagi T, Takahashi M, Abdel-Aleem H, Ikeuchi K (2014) Microstructural evolution and mechanical properties of high strength 3–9% Ni-steel alloys weld metals produced by electron beam welding. *Mater Des* 60:391–400. <https://doi.org/10.1016/j.matdes.2014.03.056>
 38. Navarro-López A, Hidalgo J, Sietsma J, Santofimia MJ (2017) Characterization of bainitic/martensitic structures formed in isothermal treatments below the Ms temperature. *Mater Charact* 128:248–256. <https://doi.org/10.1016/j.matchar.2017.04.007>
 39. Gáspár M, Balogh A, Sas I (2015) Physical simulation aided process optimisation aimed sufficient HAZ toughness for quenched and tempered AHSS. IIW International Conference High-Strength Materials - Challenges and Applications
 40. Li X, Shang C, Ma X, Subramanian SV, Misra RDK, Sun J (2018) Structure and crystallography of martensite-austenite constituent in the intercritically reheated coarse-grained heat affected zone of a high strength pipeline steel. *Mater Charact* 138:107–112. <https://doi.org/10.1016/j.matchar.2018.01.042>
 41. Afkhami S (2018) Investigation on the weldability of cold-formed ultra-high strength steels S700mc and S1100. Lappeenranta University of Technology
 42. Wang XL, Nan YR, Xie ZJ, Tsai YT, Yang JR, Shang CJ (2017) Influence of welding pass on microstructure and toughness in the reheated zone of multi-pass weld metal of 550 MPa offshore engineering steel. *Mater Sci Eng A* 702:196–205. <https://doi.org/10.1016/j.msea.2017.06.081>
 43. Li X, Ma X, Subramanian SV, Shang C, Misra RDK (2014) Influence of prior austenite grain size on martensite-austenite constituent and toughness in the heat affected zone of 700MPa high strength linepipe steel. *Mater Sci Eng A* 616:141–147. <https://doi.org/10.1016/j.msea.2014.07.100>
 44. Li X, Shang C, Ma X, Gault B, Subramanian SV, Sun J, Misra RDK (2017) Elemental distribution in the martensite-austenite constituent in intercritically reheated coarse-grained heat-affected zone of a high-strength pipeline steel. *Scr Mater* 139:67–70. <https://doi.org/10.1016/j.scriptamat.2017.06.017>
 45. Kumar S, Nath SK, Kumar V (2015) Effect of single and multiple thermal cycles on microstructure and mechanical properties of simulated HAZ in low carbon bainitic steel. *Mater Perform Charact* 4:365–380. <https://doi.org/10.1520/MPC20150007>
 46. Chen L, Nie P, Qu Z, Ojo OA, Liqian X, Zhuguo L, Huang J (2020) Influence of heat input on the changes in the microstructure and fracture behavior of laser welded 800MPa grade high-strength low-alloy steel. *J Manuf Process* 50:132–141. <https://doi.org/10.1016/j.jmapro.2019.12.007>
 47. Tasalloti H, Kah P, Martikainen J (2017) Effect of heat input on dissimilar welds of ultra high strength steel and duplex stainless steel: microstructural and compositional analysis. *Mater Charact* 123:29–41. <https://doi.org/10.1016/j.matchar.2016.11.014>

Publisher's note Springer Nature remains neutral with regard to jurisdictional claims in published maps and institutional affiliations.